A Three-Axis CMOS-MEMS Accelerometer Structure With Vertically Integrated Fully Differential Sensing Electrodes

Ming-Han Tsai, Yu-Chia Liu, and Weileun Fang, *Senior Member, IEEE*

Abstract—This study presents a novel CMOS-microelectromechanical systems (MEMS) three-axis accelerometer design using Taiwan Semiconductor Manufacturing Company 0.18-μm one-poly-Si six-metal/dielectric CMOS process. The multilayer metal and dielectric stacking features of the CMOS process were exploited to vertically integrate the in-plane and out-of-plane capacitive sensing electrodes. Thus, the three-axis sensing electrodes can be integrated on a single proof mass to reduce the footprint of the accelerometer. Moreover, the fully differential gap-closing sensing electrodes among all three axes are implemented to increase the sensitivities and decrease the noise. The in-plane and out-of-plane sensing gaps are respectively defined by the minimum metal line width and the thickness of one metal layer by means of the metal wet-etching post-CMOS process. Thus, the capacitive sensitivities are further improved. The fully differential gap-closing sensing electrodes also bring the advantage of reduced cross talks between all three axes. As a result, the footprint of the presented three-axis accelerometer structure is only 400×400 μm^2. Compared with existing commercial or CMOS-MEMS studies, the size is significantly reduced. The measured sensitivities (nonlinearities) are 14.7 mV/G (3.2%) for the X-axis, 15.4 mV/G (1.4%) for the Y-axis, and 14.6 mV/G (2.8%) for the Z-axis. [2012-0044]

Index Terms—Accelerometer, CMOS microelectromechanical systems (MEMS), cross talks, fully differential, post-CMOS process.

I. Introduction

THE microelectromechanical systems (MEMS) accelerometer is an important device for motion sensing and has found various applications in automobile, industry, and consumer electronics [1]. The three-axis accelerometer (X-, Y-, and Z-axes) has been extensively exploited to detect the linear motion of an object in space. The three-axis MEMS accelerometer has also been frequently used to detect the inclined angles of bulky structures in the industrial field. Other industrial applications using multiaxis MEMS accelerometers are vibration and motion monitoring [2], robot positioning and control [3], etc.

It is straightforward to package two to three discrete chips to achieve the three-axis accelerometer [4]. Presently, with the increasing demand of motion sensing in different applications, small chip size becomes a critical concern for micromachined accelerometer design. The monolithic integration of three sensing units (three proof masses) on a single chip can reduce the size of the three-axis accelerometer [5]. The total chip size can be further shrunk by reducing the number of proof masses for the three-axis accelerometer [6]; however, the electrical routing becomes a critical concern. To overcome the electric routing problem, the logic signal processing has been employed to achieve a single-proof-mass bulk micromachined three-axis accelerometer [7], [8]. The bonding process has been adopted to integrate three-axis sensing electrodes [9]. The poly-Si-based surface micromachining process provides a better electrical routing ability to realize the single-proof-mass three-axis accelerometers [10], [11]. The size of the mechanical structure can be shrunk to 800×800 μm^2. Nevertheless, the fully differential sensing structure in all three sensing directions is not yet available.

Using an available CMOS process foundry is considered as a promising approach to implement MEMS accelerometers. Such technology has the advantages of mature foundry service for mass production and monolithic integration with sensing electronics to shrink the chip size and reduce the parasitic capacitance [12]. A monolithic integration of three accelerometers for a different sensing axis has been presented by the 0.35-μm Taiwan Semiconductor Manufacturing Company (TSMC) CMOS process [13]. CMOS-MEMS capacitive three-axis accelerometers with fully differential sensing electrodes have been reported in [6], [14], and [15]. The sensing electrodes are distributed along the edges of the proof mass and supporting frame. The large single-proof-mass accelerometer design (700×700 μm^2) is employed in [6] to arrange the sensing electrodes by three individual frames. The accelerometer with a large suspension structure suffers from serious unwanted predeformations induced by thin-film residual stresses. Thus, the sensitivity of such an accelerometer is poor. To reduce the size of the accelerometer, a single-proof-mass accelerometer design

M.-H. Tsai is with Pixart Imaging Inc., Hsinchu 30078, Taiwan, and also with the Institute of NanoEngineering and MicroSystems, National Tsing Hua University, Hsinchu 30013, Taiwan (e-mail: d9635816@oz.nthu.edu.tw).

Y.-C. Liu is with the Institute of NanoEngineering and MicroSystems, National Tsing Hua University, Hsinchu 30013, Taiwan (e-mail: s9835804@m98.nthu.edu.tw).

W. Fang is with the Institute of NanoEngineering and MicroSystems and the Department of Power Mechanical Engineering, National Tsing Hua University, Hsinchu 30013, Taiwan (e-mail: fang@pme.nthu.edu.tw).

This article has been accepted for inclusion in a future issue of this journal. Content is final as presented, with the exception of pagination.

2   JOURNAL OF MICROELECTROMECHANICAL SYSTEMS

$(400 \times 400\ \mu m^2)$ is presented in [14]. In this design, all three-axis sensing electrodes are distributed along the limited space on such small proof mass. As a result, the total number of sensing electrodes as well as the sensitivities of accelerometer is reduced. In summary, the designs of [6] and [14] presented by the authors' group encountered the tradeoff between size and sensing signal. A complicated double-sided post-CMOS process is required for the single-proof-mass accelerometer design in [15].

This paper presents the design of a three-axis accelerometer based on the standard TSMC 0.18-μm one-poly-Si six-metal/ dielectric (1P6M) CMOS process [16]. Due to the multilayer metal and dielectric features, the in-plane and out-of-plane fully differential sensing electrodes can be vertically integrated. In other words, the sensing electrodes can be distributed not only along the width/length but also along the thickness of the proof mass. Thus, the number of sensing electrodes can be significantly increased. Moreover, the fully differential gap-closing three-axis sensing electrodes can be realized on a single proof mass. The metal wet-etching post-CMOS process is employed to define the structures and in-plane and out-of-plane sensing gaps. Thus, the sensing gap is not limited by the aspect ratio and can be reduced with CMOS line width ability.

II. DESIGN CONCEPT

As shown in Fig. 1(a), the proposed accelerometer design consists of a proof mass, springs, supporting frames, and sensing electrodes. The movable sensing electrodes are fixed to the proof mass, whereas the stationary sensing electrodes are connected to the supporting frame which are anchored to the substrate. This accelerometer is implemented using the commercially available standard TSMC 0.18-μm 1P6M CMOS process. Fig. 1(b) shows the standard layer stacking of the CMOS process, including one layer of poly-Si, six layers of metal, dielectric, and tungsten vias. As compared with the standard 0.35-μm two-poly-Si four-metal (2P4M) CMOS process, the proposed 0.18-μm 1P6M CMOS process not only offers a smaller line width but also provides more metal and dielectric layers for MEMS structure design. The total thickness of thin layers available for the MEMS structure reaches 8.8 μm (not including the passivation). Moreover, the 0.18-μm CMOS process offers the advantages of reducing circuit size and providing more circuit functions than the 0.35-μm one. Note that the dimensions of the accelerometer have to meet the rules and specifications of the standard processes, such as the film thickness and the minimum line width.

Fig. 1(c) shows the cross-sectional view of AA′ shown in Fig. 1(a). It shows all thin layers on top of the substrate, as shown in Fig. 1(b), that are employed to form the proof mass. In other words, the total thickness of the proof mass is 8.8 μm. Thus, the proof mass as well as the sensitivity of the accelerometer is increased, as compared with the accelerometer implemented using the TSMC 0.35-μm 2P4M CMOS process [6], [14]. In this paper, the typical planar dimensions of the proof mass are $250 \times 250\ \mu m^2$. Fig. 1(d) shows the cross section of BB′ shown in Fig. 1(a). The spring structure only consists of Metal-1 and Metal-2 layers to lower its stiffness in the out-of-plane direction. The total spring thickness is
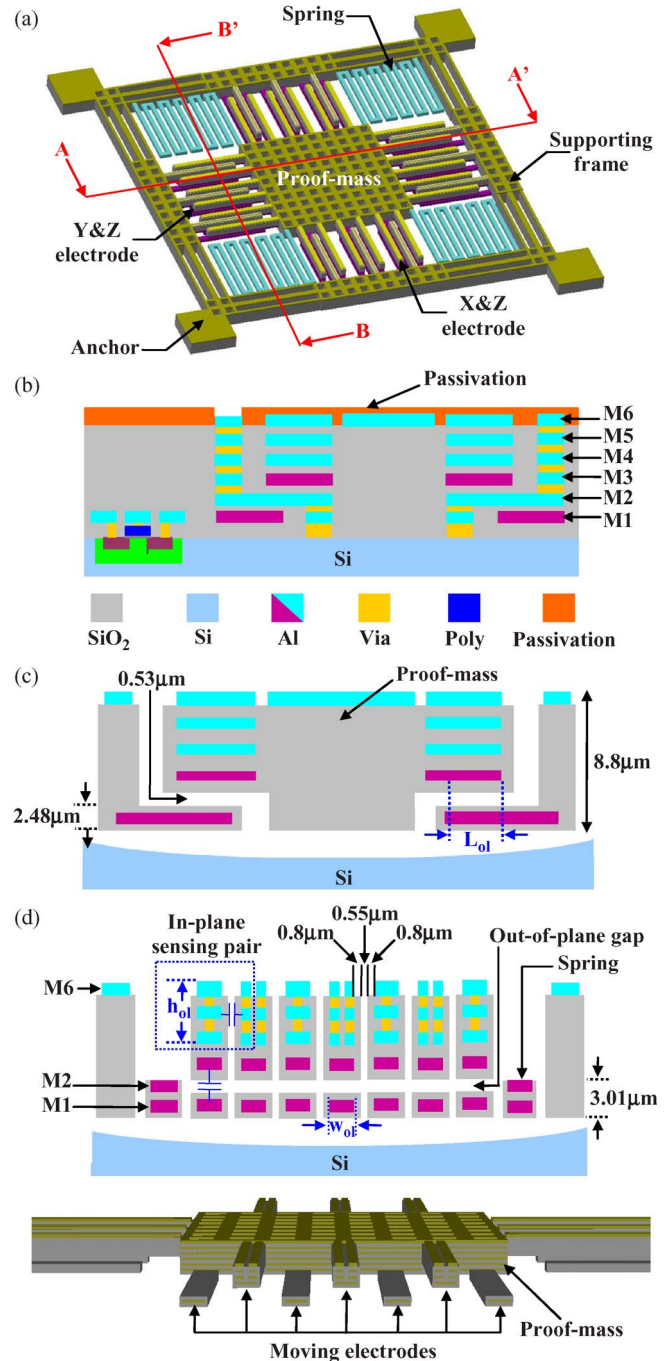

Fig. 1. (a) Schematic illustration of the proposed three-axis accelerometer, (b) the layer stacking of the 0.18-μm 1P6M CMOS process to implement the proposed accelerometer, (c) the AA′ cross-sectional view, and (d) the BB′ cross-sectional view and the distribution of moving electrodes on the proof mass.

designed as 3.01 μm. The stiffnesses of the serpentine spring are simulated to be 0.79 (x-axis), 0.76 (y-axis), and 1.48 N/m (z-axis) as shown in Fig. 2. The typical planar dimensions of the components, including proof mass, springs, supporting frame, and sensing electrodes, shown in Fig. 1(a) are $400 \times 400\ \mu m^2$. Moreover, the fully differential gap-closing sensing scheme has been implemented in both in plane and out of plane of the proposed three-axis accelerometer design. As shown in Fig. 1(d), the in-plane and out-of-plane sensing electrodes are integrated vertically to reduce the structure size. The design details are discussed in the following subsections.
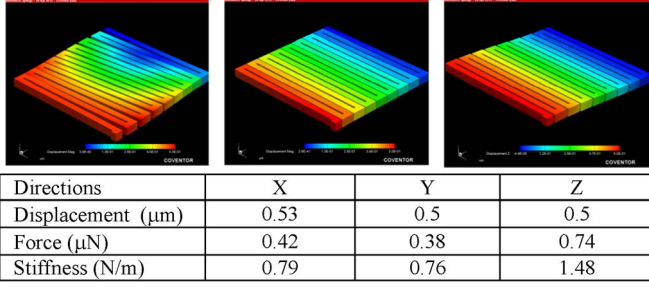
Directions	X	Y	Z
Displacement (μm)	0.53	0.5	0.5
Force (μN)	0.42	0.38	0.74
Stiffness (N/m)	0.79	0.76	1.48

Fig. 2. Spring stiffness simulation results.

TABLE I
SENSING ELECTRODE DESIGN AND THE PREDICTED
SENSING CAPACITANCE AND SENSITIVITY FOR THE
PROPOSED THREE-AXIS ACCELEROMETER

Parameters	X-electrodes	Y-electrodes	Z-electrodes
Electrodes number	72	72	144
Overlap length, L_{ol} (μm)	45	45	45
Overlap thickness, h_{ol} (μm)	4.1	4.1	
Overlap width, w_{ol} (μm)			4.5
Effective sensing gap, d (μm)	0.95	0.95	0.96
Sensing capacitance (fF)	222.5	222.5	495.8
Capacitance change sensitivity (fF/G)	2.46	2.46	2.68

A. Vertically Integrated Sensing Electrodes

As shown in Fig. 1(d), the sensing electrodes are distributed in both in-plane and out-of-plane directions. Thus, the in-plane (X- and Y-axes) and out-of-plane (Z-axis) accelerations can be detected by means of the gap-closing approach. The top three metal layers (Metal-4–Metal-6) are used as the in-plane sensing electrodes, and these metal layers are electrically connected using the tungsten vias. The in-plane acceleration will cause the change of air gap and lead to the capacitance change of sensing electrodes. As shown in Fig. 1(a), the electrodes parallel to BB′ form the in-plane differential sensing unit to detect the X-axis acceleration, and those parallel to AA′ can detect the Y-axis acceleration. Moreover, the Metal-1 and Metal-3 layers are employed as the out-of-plane sensing electrodes. The out-of-plane acceleration will cause the change of air gap and lead to the capacitance change of sensing electrodes. Metal-1 and Metal-3 act as the top and bottom sensing electrodes, respectively, and Metal-2 is used as the sacrificial layer to define the out-of-plane sensing gap. In addition, the Metal-3 (for out-of-plane sensing) and Metal-4 (for in-plane sensing) layers are well insulated by the dielectric layer of the CMOS process.

This study employs the metal thin films as the sacrificial layers to define the sensing gaps. The sensing gaps are formed after etching the sacrificial metal layers. Thus, as shown in Fig. 1(d), the minimum metal and via line widths of the 0.18-μm CMOS process are exploited to reduce the in-plane air gap. Since the dielectric layer is used as the protection layer during the sacrificial metal etching, the in-plane sensing gap includes not only the air gap but also the dielectric protection layer. Ideally, the sensing gap between each in-plane sensing pair consists of a 0.55-μm-wide air gap and two 0.80-μm-wide SiO$_2$ layers, as shown in Fig. 1(d). Since the dielectric constant of SiO$_2$ is near 4.0, the equivalent sensing gap d_{eq} (under vacuum) is determined by [17]

$$d_{eq} = \frac{d_{air}}{\varepsilon_{air}} + \frac{2d_{SiO_2}}{\varepsilon_{SiO_2}} \tag{1}$$

where d_{air} and ε_{air} are the gap and relative dielectric constant of air, respectively, and d_{SiO2} and ε_{SiO2} are the gap and relative dielectric constant of SiO$_2$, respectively. Thus, the equivalent in-plane sensing gap determined from (1) is 0.95 μm. Similarly, the sensing gap between each out-of-plane sensing pair consists of a 0.53-μm air gap (defined by Metal-2 layer thickness) and

two 0.85-μm-thick SiO$_2$ layers employed to protect Metal-1 and Metal-3 during the sacrificial metal etching. Thus, the equivalent out-of-plane sensing gap determined from (1) is 0.96 μm. The vertically integrated in-plane and out-of-plane sensing electrodes have the same planar dimensions (55 μm in length and 4.5 μm in width). In addition, the stationary and moving electrodes have an overlap length L_{ol} of 45 μm for both in-plane and out-of-plane sensing electrodes. Thus, the in-plane sensing area is determined by the overlap area $h_{ol} \times L_{ol}$ of the three metal layers and two dielectric layers (Metal-4–Metal-6) between moving and stationary electrodes, and the out-of-plane sensing area $w_{ol} \times L_{ol}$ is defined by the overlap area of the top electrodes (Metal-3) and bottom electrodes (Metal-1). For in-plane sensing capacitance, the electric field is not only in the side wall area of metal layers but also in the area in the width direction, the metal layers, and fringes of metal and oxide layers. For out-of-plane sensing electrodes, the overlap area of metal layers is larger than the in-plane one. The side wall and the fringe of metal and oxide layers also contribute to out-of-plane sensing capacitance. This study constructed the 3-D model of sensing electrodes and used finite element method to simulate the sensing capacitance more precisely. Thus, the total initial sensing capacitances are simulated to 222.5 fF for the X- and Y-axes and 495.8 fF for the Z-axis. Moreover, the capacitance changes for both in-plane and out-of-plane directions are designed to be similar by varying the spring stiffness. The predicted sensitivities (capacitance change with acceleration) in in-plane and out-of-plane directions are 2.46 and 2.68 fF/G, respectively. Table I summarizes the detailed design parameters of the three-axis sensing electrodes.

In comparison, the structure design in [6] is based on the 2P4M process. As limited by the number of electrical layers, the sensing electrodes are distributed along each edge of the proof mass, and supporting frames can only detect the acceleration of one axis. Thus, the chip size is significantly increased by supporting frames for the requirement of planar-integrated sensing electrodes, as shown in Fig. 3. As indicated, this study exploits the 1P6M process to design the vertically integrated sensing electrodes. Thus, the sensing electrodes distributed along each edge of the proof mass can detect two axes. As a result, supporting frames are not required, and then, the structure size of the accelerometer is significantly reduced without sacrificing the performance.
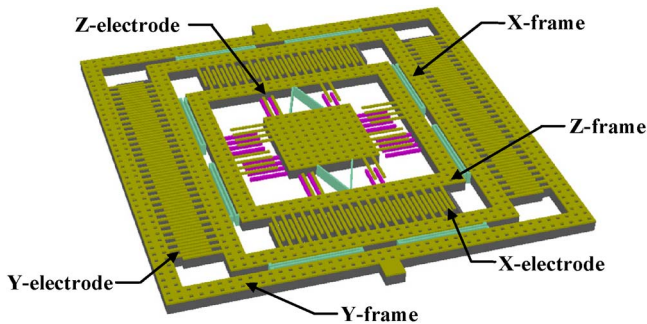
Fig. 3.   Planar integration of three-axis sensing electrode design in [6].
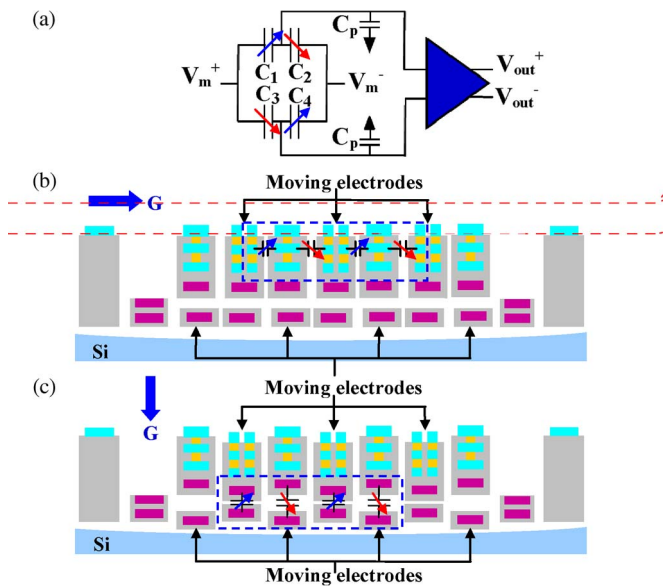

Fig. 4.   (a) Schematic of the fully differential sensing structure, (b) the in-plane fully differential sensing electrodes, and (c) the out-of-plane fully differential sensing electrode design.

Fig. 5.   Routings of the three-axis fully differential sensing structure.

B. Three-Axis Fully Differential Sensing Structure

This study exploits the six metal and dielectric layers of the TSMC 0.18-μm CMOS process for electrical routings. Thus, the fully differential sensing design for all three axes can be realized to reduce the noise level and increase the sensitivity, as shown in Fig. 4(a). The in-plane and out-of-plane CMOS-MEMS fully differential sensing accelerometer designs have been reported in [18] and [19]. To reduce the space of the accelerometer, this study proposed the in-plane and out-of-plane fully differential sensing electrode design, as shown in Fig. 3(b) and (c). As the in-plane acceleration acts on the sensing electrodes, the moving electrodes would have a corresponding in-plane displacement as shown in Fig. 4(b). The gap change between moving electrodes and two adjacent stationary electrodes would simultaneously induce increasing and decreasing capacitance changes to form the in-plane fully differential sensing pair. Similarly, as the Z-axis acceleration acts on the accelerometer, the out-of-plane displacement of the proof mass would also change the gaps between each sensing electrode pair. As shown in Fig. 4(c), the accelerometer expe-
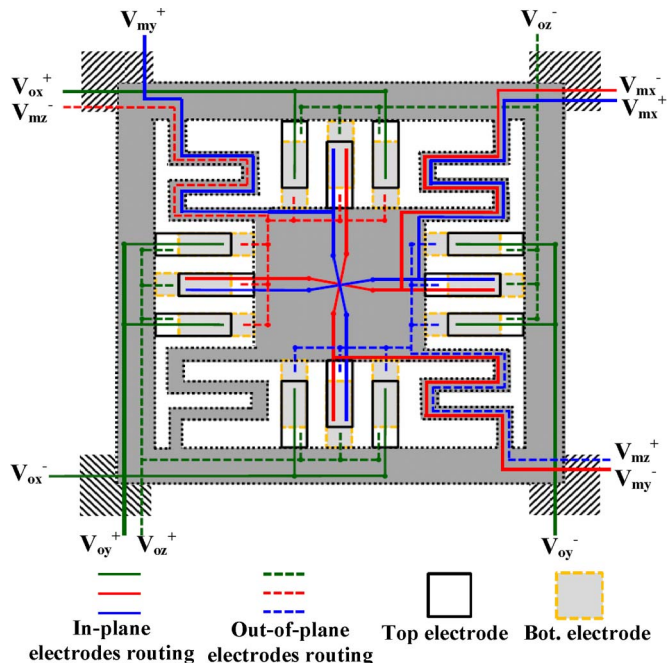
riences a downward Z-axis acceleration, and the top moving electrode moves toward the stationary electrode underneath to increase the sensing capacitance. On the other hand, the bottom moving electrode moves away from the stationary electrode, and the sensing capacitance is decreased. As a result, these out-of-plane sensing electrodes form the fully differential gap-closing sensing structure.

In this paper, the three-axis fully differential sensing structure requires, in total, 12 wires to route from the accelerometer structure to the sensing circuit and input modulation pad. The metal layers from Metal-1 to Metal-5 are used for the routing of sensing and modulation signals, and the M6 layer is for grounding. The routing schematic is shown in Fig. 5. Since the flexible spring only consists of Metal-1 and Metal-2 layers, each spring can only provide two metal wires for routing. The modulation signals ($V_{mx}^{+}, V_{mx}^{-}, V_{my}^{+}, V_{my}^{-}, V_{mz}^{+}$, and V_{mz}^{-}) are input from the bonding pads through springs and proof mass to the sensing electrodes. In addition, the out-of-plane sensing signals are routed by the Metal-1 and Metal-3 layers, and the in-plane sensing signals are routed by the Metal-4 and Metal-5 layers. Moreover, the tungsten via allows the switching of signals among metal layers to increase the routing flexibility. Finally, the sensing signals ($V_{ox}^{+}, V_{ox}^{-}, V_{oy}^{+}, V_{oy}^{-}, V_{oz}^{+}$, and V_{oz}^{-}) are output from the sensing electrodes through the supporting frame to bonding pads. The parasitic capacitance is mainly coming from the substrate under the accelerometer structure and wire routings. The silicon isotropic etching can increase the distance between sensing electrodes and substrate. Thus, as compared with the sensing capacitance, the parasitic capacitance is relatively small.

X and Y Sensing Coupled to the Z-Axis Acceleration: Since the in-plane and out-of-plane sensing electrodes are vertically
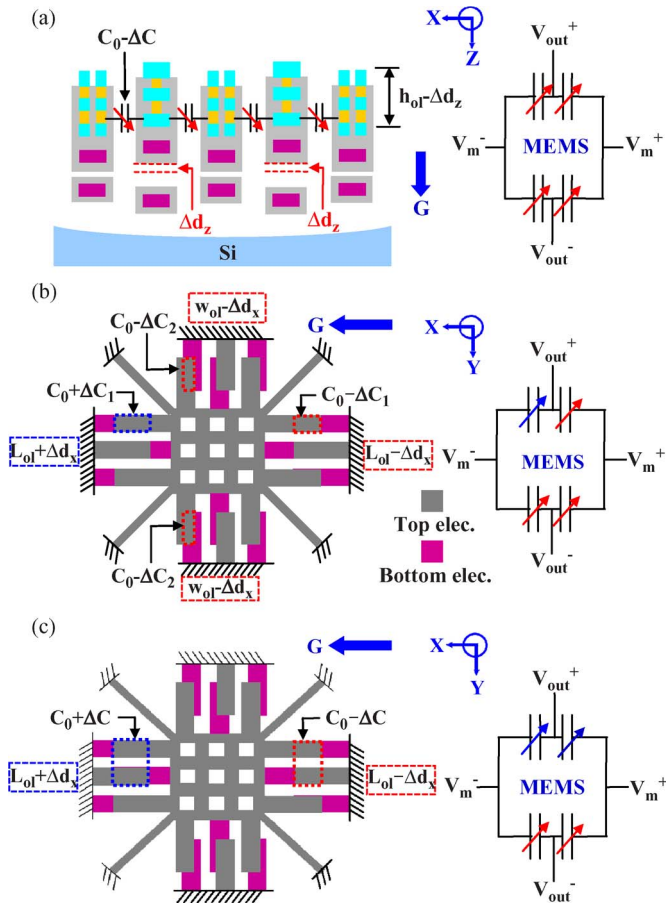
This article has been accepted for inclusion in a future issue of this journal. Content is final as presented, with the exception of pagination.

TSAI *et al.*: THREE-AXIS CMOS-MEMS ACCELEROMETER STRUCTURE WITH SENSING ELECTRODES

5

Fig. 6. Coupling of the sensing electrodes. (a) X- and Y-axis capacitance change induced by the Z-axis acceleration. (b) Z-axis capacitance change induced by the X- and Y-axis acceleration. (c) X-axis (Y-axis) capacitance change induced by the Y-axis (X-axis) acceleration.

integrated, the coupling problem among each sensing axis is a concern. The proposed fully differential sensing electrode design also has the advantage of cross-talk canceling. For instance, when the moving electrode has an out-of-plane displacement Δd_z caused by the Z-axis acceleration, the overlap area for all in-plane sensing electrodes decreases from $h_{\rm ol} \times L_{\rm ol}$ to $(h_{\rm ol} - \Delta d_z) \times L_{\rm ol}$, as shown in Fig. 6(a). Such vertical comb-type single-ended capacitance change is considered as the common mode and canceled.

Z-Axis Sensing Coupled to the X- and Y-Axis Acceleration: When the moving electrode has an in-plane displacement Δd_x caused by the X-axis acceleration, the top and bottom out-of-plane sensing electrodes would also experience a capacitance change induced by the area change, as shown in Fig. 6(b). The overlap area of the out-of-plane sensing electrodes (for the $X-Z$ pair) decreases from $w_{\rm ol} \times L_{\rm ol}$ to $(w_{\rm ol} - \Delta d_x) \times L_{\rm ol}$. Meanwhile, the overlap area of out-of-plane sensing electrodes (for the $Y-Z$ pair) respectively changes from $w_{\rm ol} \times L_{\rm ol}$ to $w_{\rm ol} \times (L_{\rm ol} - \Delta d_x)$ and $w_{\rm ol} \times (L_{\rm ol} + \Delta d_x)$, as shown in Fig. 6(b). Such capacitance changes cannot be canceled by the fully differential sensing design and will induce a cross-talk signal ΔC_{zx} (or ΔC_{zy}). However, the ratio of ΔC_{zx} (or ΔC_{zy}) and the capacitance change ΔC_z induced by the Z-axis gap sensing electrodes are $(w_{\rm ol} \times d_z/h_{\rm ol} \times L_{\rm ol})$, where d_z is the
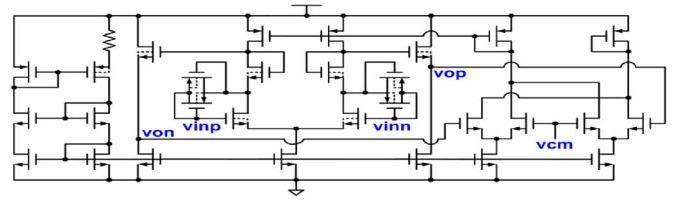

Fig. 7. Architecture of the CTV preamplifier.

Z-axis sensing gap. Hence, the cross-talk signal is calculated to be 1.2% of the sensing signal using (2)

$$\frac{\Delta C_{zx}}{\Delta C_x}$$
$$= \frac{((C_0 + \Delta C_1) - (C_0 - \Delta C_2)) - ((C_0 - \Delta C_1) - (C_0 - \Delta C_2))}{\Delta C_x}$$
$$= \frac{\Delta C_1 + \Delta C_2 + \Delta C_1 - \Delta C_2}{\Delta C_x} = \frac{w_{\rm ol} \times d_z}{2 \times L_{\rm ol} \times h_{\rm ol}}. \quad (2)$$

X-Axis (Y-Axis) Sensing Coupled to the Y-Axis (X-Axis) Acceleration: The cross talk between in-plane sensing axes (X- and Y-axes) can be decoupled by the fully differential sensing design as well. For instance, when the moving electrode has an in-plane displacement Δd_x caused by the X-axis acceleration, the Y-axis in-plane sensing electrodes would also experience an in-plane displacement Δd_x. As shown in Fig. 6(c), the Y-axis sensing electrodes at the left-hand and right-hand sides of the proof mass, respectively, have the overlap area change of $h_{\rm ol} \times (L_{\rm ol} + \Delta d_x)$ and $h_{\rm ol} \times (L_{\rm ol} - \Delta d_x)$. The capacitance changes of sensing electrodes are also shown in Fig. 6(c). Such capacitance change of sensing electrode pairs can be canceled by the fully differential sensing mechanism [6].

This study employed the continuous-time voltage (CTV) sensing mechanism to reduce the noise folding problem. The architecture of the CTV preamplifier as shown in Fig. 7 includes first stage with source follower and common mode feedback (CMFB) to adjust output dc level. In order to minimize the flicker noise, the sensing signal was modulated to a higher frequency. With 20-pF 10-kΩ load simulation, the preamplifier achieves about 30-dB open-loop gain with a 10-MHz 3-dB bandwidth, and input-referred noise is 26 nV/rtHz at 1-MHz modulation frequency.

III. FABRICATION PROCESS AND RESULTS

The proposed accelerometer was implemented using the TSMC 0.18-μm 1P6M standard 8-in CMOS process and the post-CMOS micromachining process. The post-CMOS process was done in the Center for Nanotechnology, Materials Science, and Microsystems, National Tsing Hua University. After the device design, the thin films were patterned and stacked by the standard CMOS process, as shown in Fig. 8(a). The metal and dielectric films were covered with the passivation layer except the regions for the following metal wet etching. After that, the post-CMOS etching processes were employed to release the micromechanical structures, as shown in Fig. 8(b)–(d). Fig. 8(b) shows the metal wet-etching process using the H$_2$SO$_4$ and H$_2$O$_2$ solution to remove the aluminum and tungsten via. The etching was initiated from the exposed aluminum film, and
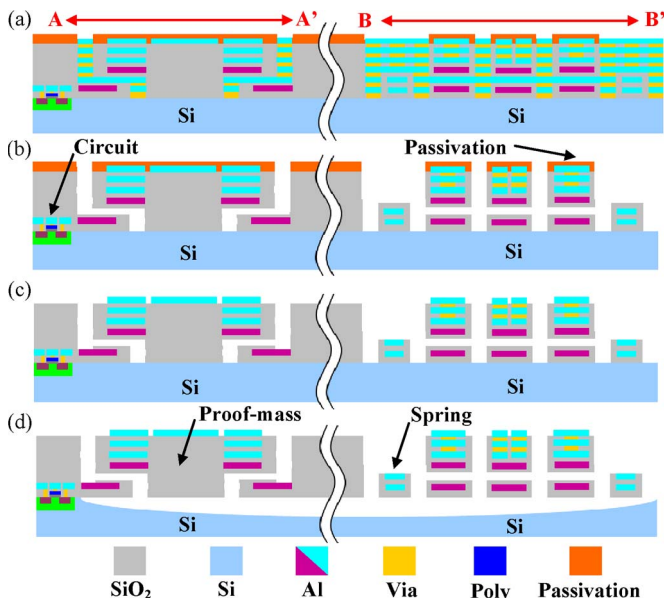
Fig. 8. Fabrication processes. (a) Chip fabricated by the TSMC 0.18-μm 1P6M CMOS process. (b) Metal wet etching to define the MEMS structures and the sensing gaps. (c) RIE to remove the passivation for wire bonding. (d) XeF$_2$ to etch the Si substrate and release the MEMS structures.

the dielectric films were used as the etching protection layer. The in-plane and out-of-plane sensing gaps and the shape of micromechanical structures were defined in this step. Since the structure remained fixed on the substrate after the metal wet etching, the stiction problem of the submicrometer gaps was prevented. Reactive ion etching (RIE) was then employed to remove the passivation to expose the pad for wire bonding, as shown in Fig. 8(c). Finally, the XeF$_2$ silicon isotropic etching [20] was used to release the structure as shown in Fig. 8(d).

The scanning electron microscope (SEM) micrographs in Fig. 9 show the typical fabrication results of the three-axis accelerometer. The spring, proof mass, supporting frame, and sensing electrodes are observed in Fig. 9(a). The zoom-in micrograph in Fig. 9(b) shows the top view of the sensing electrode array. Fig. 9(c) further shows the zoom-in micrograph of the submicrometer air gap between the in-plane electrodes. The zoom-in micrograph in Fig. 9(d) shows the vertically integrated sensing electrodes. The submicrometer air gap between the out-of-plane sensing electrodes is also observed. The optical image of Fig. 10(a) shows the monolithic integration of the single-proof-mass three-axis accelerometer and the sensing circuits. The sensing circuits were covered with the transparent dielectric films and can be observed by the optical microscope. The fabricated accelerometer was characterized after being wire bonded on the ceramic package, as shown in Fig. 10(b).

IV. MEASUREMENT RESULTS

The accelerometer was driven using the built-in electrostatic actuators to characterize its resonant frequencies of three different axes. The in-plane and out-of-plane dynamic responses were respectively detected using the commercial stroboscope micromotion analyzer (Etec Inc., MMA G2) and laser Doppler vibrometer (GRAPHTEC Corporation, AT0041). The measured resonant frequencies for the X-, Y-, and Z-axes
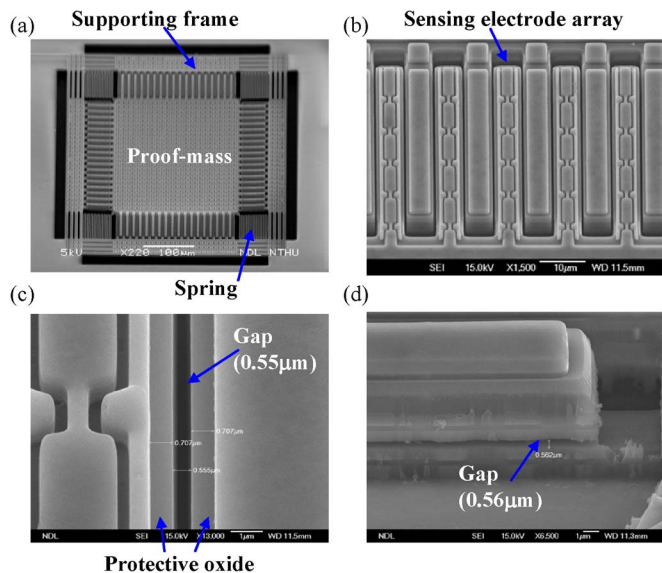

Fig. 9. SEM micrographs of typical fabrication results. (a) 400×400 μm^2 accelerometer (not including sensing circuits). (b) Sensing electrode array. (c) Zoom-in micrograph to show the submicrometer in-plane sensing gap defined by the sacrificial metal layer and the protective oxide layer. (d) Out-of-plane sensing electrode and gap.
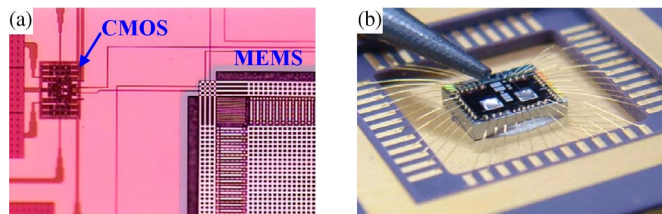

Fig. 10. Optical micrographs of typical fabricated and packaged accelerometers. (a) Three-axis accelerometer with monolithically integrated sensing circuits and (b) the accelerometer chip after being wire bonded and packaged on a ceramic housing.

are 7.1, 6.1, and 10.6 kHz, respectively. Despite the increase of stacking layers for the presented accelerometer, the released structure still bent by the residual stresses of metal and dielectric films. According to the measurement from the commercial optical interferometer (VEECO Inc., NT1100), the released proof mass bends with a 4.5-mm radius of curvature. In order to compensate the curvature, the stress compensation frame is used [21]. The stress compensation frame is a suspended structure which is anchored at the same location with springs and mass structure. Due to thin-film residual stresses, the suspended spring, proof mass, and frame could be bent out of plane. Thus, the sensing electrodes on the bent proof mass will experience an unwanted out-of-plane displacement. Since the proof mass and the compensation frame have the same film stacking, their bending curvatures due to thin-film residual stresses are the same. Thus, sensing electrodes on the frame also experience a similar out-of-plane displacement as those on the proof mass. As a result, the unwanted out-of-plane displacement of sensing electrodes on the proof mass can be compensated by the bending deformation of the compensation frame.

The accelerometer was then integrated with various passive components, such as tunable resistor, capacitor, and ICs, on a printed circuit board for CMFB voltage, as shown in Fig. 11(a).
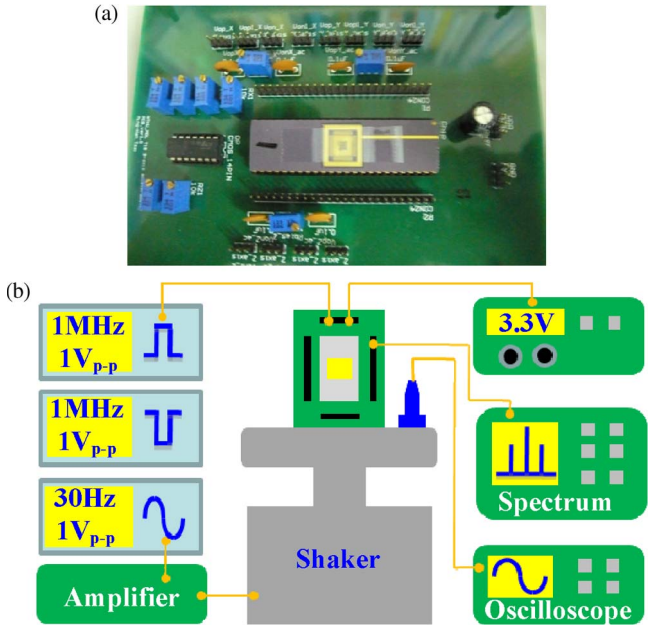
Fig. 11.   (a) Packaged accelerometer mounted on a printed circuit board for testing and (b) the measurement setup.
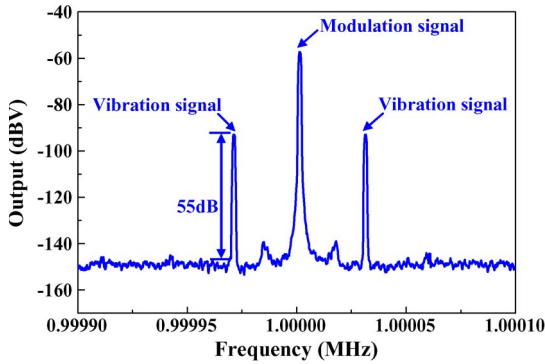

Fig. 12.   Typical spectrum output from the accelerometer after the excitation of 1 G and 30 Hz by the shaker.

The measurement setup to characterize the accelerometer on a printed circuit board is shown in Fig. 11(b). The input acceleration is generated by the shaker (B&K Corporation, LDS V406) and controlled by the function generator. The input acceleration is calibrated by the commercial piezo accelerometer (PCB PIEZOTRONICS Inc., Model 352C44). The output signal is monitored and recorded by the oscilloscope and spectrum analyzer. The output dc level is 1.65 V which is adjusted by the tunable resistor on a printed circuit board. Two antiphase square waves with 1 MHz and 1 V_{p-p} are injected as the modulation signals to minimize the flicker noise. Fig. 12 shows the X-axis output signal recorded by the spectrum analyzer, as the accelerometer was operated under a 1-G 30-Hz excitation. The center peak resulted from the input modulation, and the signal-to-noise ratio reaches 55 dB. Measured noises for three sensing axes are 2.1 mG/rtHz for the X-axis, 2.0 mG/rtHz for the Y-axis, and 2.1 mG/rtHz for the Z-axis. As shown in Fig. 13, this study has characterized the output voltage of the accelerometer as the acceleration ranging from 10 mG to 1 G. Thus, the sensitivities (nonlinearities) determined from the linear data fitting of the measurements are 14.7 mV/G (3.2%) for
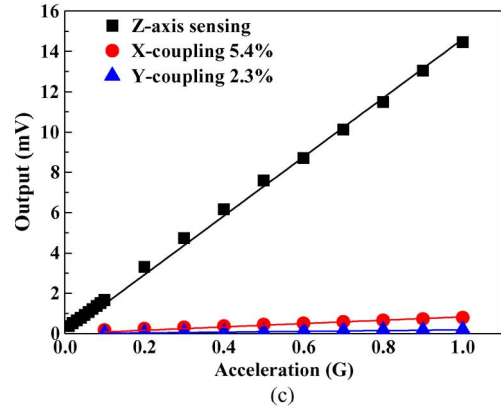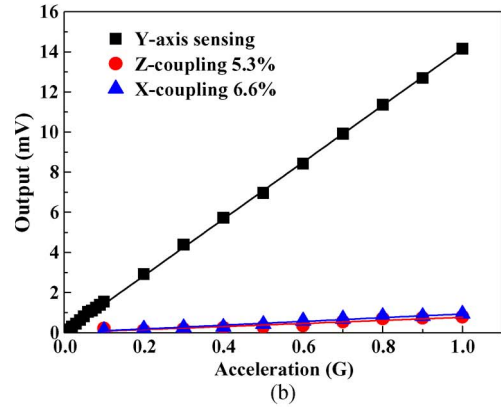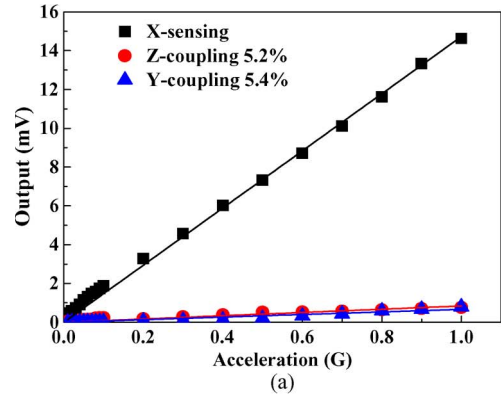

Fig. 13.   Typical measured output voltages and cross-talk signals at different accelerations. (a) X-axis acceleration, (b) Y-axis acceleration, and (c) Z-axis acceleration.

the X-axis, 15.4 mV/G (1.4%) for the Y-axis, and 14.6 mV/G (2.8%) for the Z-axis. As the initial capacitance and sensing gap are the same as expected, the sensitivity should be inversely proportional to the square of its resonant frequency. However, the initial sensing capacitance and sensing gap could be influenced by the predeformation of the suspended MEMS structures. Thus, the resonant frequency is not the only factor to determine the sensitivity of the accelerometer. This is the reason that the Y-axis sensitivity is only 5% higher than that of the X-axis despite the 16% difference of their natural frequency. From the measurement results, it is obvious that cross talk is not perfectly cancelled as expected. Ideally, the cross talk can be cancelled through the arrangement of sensing electrodes. For instance, as shown in Fig. 6(b), the X-axis acceleration will cause an area change ΔA of the Z-axis

TABLE II
SUMMARY OF THE MEASUREMENT RESULTS

Specification	X-axis	Y-axis	Z-axis
Range (G)	0.01~1	0.01~1	0.01~1
Sensitivity (mV/G)	14.7	15.4	14.6
Non-linearity (%)	3.2	1.4	2.8
Noise (mG/√Hz)	2.1	2.0	2.1
Cross-axis sensitivity X (%)		6.6	5.4
Cross-axis sensitivity Y (%)	5.4		2.3
Cross-axis sensitivity Z (%)	5.2	5.3	

TABLE III
COMPARISON OF THE PRESENTED AND THE EXISTING
THREE-AXIS ACCELEROMETERS

Specifications	Sun et al [6]			Tsai et al [14]			This study		
Process	0.35μm 2P4M CMOS			0.35μm 2P4M CMOS			0.18μm 1P6M CMOS		
Size (mm²)	0.49			0.25			0.16		
Range (G)	0.5~6			0~3			0~1		
Sensitivity (mV/G)	X	Y	Z	X	Y	Z	X	Y	Z
	0.53	0.28	0.2	2.47	2.67	3.89	14.7	15.4	14.6
Non-linearity (%)	2.6	3.2	3.4	1.3	1.4	3.4	3.2	1.4	2.8
Noise (mG/√Hz)	120	271	357	0.59	0.59	0.8	2.1	2.0	2.1
Cross-axis (%)	<7			<9.2			<6.6		

sensing electrodes and further induce a capacitance change of $\delta C_2 (= \varepsilon A/d_z)$. According to the design and distribution of sensing electrodes, such cross-talk signal can be cancelled ($\Delta C = \Delta C_2 - \Delta C_2 = 0$), as shown in Fig. 6(b). However, as the spring or proof mass has predeformations (could be in-plane or out-of-plane deformations) caused by the thin-film residual stresses, process variation, or layout asymmetry after the process, the area change (ΔA) of sensing electrodes at different locations could be different. Moreover, the gaps of the Z-axis sensing electrodes at different locations could also be different. As a result, the cross-talk signal of the sensing electrodes shown in Fig. 6(b) cannot be cancelled and become

$$\Delta C = \frac{\varepsilon \Delta A_1}{d_1} - \frac{\varepsilon \Delta A_2}{d_2} \tag{3}$$

where ΔC is the capacitance change, ε is the dielectric constant, ΔA_1 and ΔA_2 are the changes of overlapped area, and d_1 and d_2 are the capacitive sensing gaps between the differential sensing electrodes. This is the main reason the cross talk is higher than expected.

Table II summarizes the measured performances of the proposed three-axis accelerometer. Table III lists the comparison of the presented and two existing three-axis CMOS-MEMS accelerometers. The presented accelerometer has a much smaller chip size, and its sensitivities are significantly increased for nearly one order.

V. CONCLUSION

This study has implemented a novel CMOS-MEMS accelerometer design using the standard TSMC 0.18-μm 1P6M CMOS process and post-CMOS metal wet-etching process. There are four advantages from this design: 1) The vertical integration of in-plane and out-of-plane sensing electrodes together with the single-proof-mass design significantly reduces the chip size; 2) the fully differential gap-closing sensing electrodes are implemented for all three sensing axes to provide higher sensitivity and lower noise; 3) the minimum line width and film thickness of the CMOS metal layer are exploited to respectively define the in-plane and out-of-plane sensing gaps to increase the sensitivity of the accelerometer; and 4) the cross talks among all three axes can be reduced by the fully differential scheme as well as the arrangement of sensing electrodes. The $400 \times 400\ \mu$m^2 accelerometer has been monolithically integrated with the sensing circuit. The measured sensitivities (nonlinearities) for three sensing axes are 14.7 mV/G (3.2%) for the X-axis, 15.4 mV/G (1.4%) for the Y-axis, and 14.6 mV/G (2.8%) for the Z-axis. Comparison of the performances with existing three-axis accelerometers have been summarized in Table III.

REFERENCES

[1] R. N. Dean, Jr. and A. Luque, "Application of microelectromechanical systems in industrial process and services," *IEEE Trans. Ind. Electron.*, vol. 56, no. 4, pp. 913–925, Apr. 2009.
[2] A. Albarbar, S. Mekid, A. Starr, and R. Pietruszkiewicz, "Suitability of MEMS accelerometer for condition monitoring: An experimental study," *Sensors*, vol. 8, no. 2, pp. 784–799, Feb. 2008.
[3] H. S. Liu and G. H. Pang, "Accelerometer for mobile robot positioning," *IEEE Trans. Ind. Appl.*, vol. 37, no. 3, pp. 812–819, May/Jun. 2001.
[4] Y. Zhao, F. Huang, and Z. Li, "Three-dimensional multi-chips and tri-axial sensors and method of manufacturing the same," U.S. Patent 7 536 909, May 26, 2009.
[5] M. Lemkin and B. E. Boser, "A three-axis micromachined accelerometer with a CMOS position-sense interface and digital offset-trim electronics," *IEEE J. Solid-State Circuits*, vol. 34, no. 4, pp. 456–468, Apr. 1999.
[6] C.-M. Sun, M.-H. Tsai, Y.-C. Liu, and W. Fang, "Implementation of a monolithic single proof-mass tri-axis accelerometer using CMOS-MEMS technique," *IEEE Trans. Electron Devices*, vol. 57, no. 7, pp. 1670–1679, Jul. 2010.
[7] H. Hamaguchi, K. Sugano, T. Tsuchiya, and O. Tabata, "A differential capacitive three-axis SOI accelerometer using vertical comb electrodes," in *Proc. IEEE Transducers*, Lyon, France, Jun. 2007, pp. 1483–1486.
[8] H. Takao, H. Fukumoto, and M. Ishida, "A CMOS integrated three-axis accelerometer fabricated with commercial submicrometer CMOS technology and bulk-micromachining," *IEEE Trans. Electron Devices*, vol. 48, no. 9, pp. 1961–1968, Sep. 2001.
[9] Y. Watanabe, T. Mitsui, T. Mineta, Y. Matsu, and K. Okada, "SOI micromachined 5-axis motion sensor using resonant electrostatic drive and non-resonant capacitive detection mode," *Sens. Actuators A, Phys.*, vol. 130/131, pp. 116–123, Aug. 2006.
[10] M. W. Judy and H. R. Samuels, "Inertial sensor," U. S. Patent 7 363 816, Apr. 29, 2008.

[11] A. C. McNeil, G. Li, and D. N. Koury, Jr., "Single proof mass, 3 axis MEMS transducer," U.S. Patent 6 845 670, Aug. 30, 2005.

[12] G. K. Fedder, "CMOS-based sensors," in *Proc. IEEE Sensors*, Irvine, CA, Oct. 2005, pp. 125–128.

[13] M.-H. Tsai, C.-M. Sun, C. Wang, J. Lu, and W. Fang, "A monolithic 3D fully-differential CMOS accelerometer," in *Proc. IEEE NEMS*, Sanya, China, Jan. 2008, pp. 1067–1070.

[14] M.-H. Tsai, Y.-C. Liu, C.-M. Sun, C. Wang, and W. Fang, "A CMOS-MEMS accelerometer with tri-axis sensing electrodes arrays," in *Proc. Eurosensors XXIV*, Linz, Austria, Sep. 2010, pp. 1083–1086.

[15] H. Qu, D. Fang, and H. Xie, "A monolithic CMOS-MEMS 3-axis accelerometer with a low-noise, low-power dual-chopper amplifier," *IEEE Sensors J.*, vol. 8, no. 9, pp. 1511–1518, Sep. 2008.

[16] M.-H. Tsai, Y.-C. Liu, C.-M. Sun, C. Wang, C.-W. Cheng, and W. Fang, "A $400 \times 400 \ \mu m^2$ 3-axis CMOS-MEMS accelerometer with vertically integrated fully-differential sensing electrodes," in *Proc. IEEE Transducers*, Beijing, China, Jun. 2011, pp. 811–814.

[17] C.-T. Ko, S.-H. Tseng, and M. S.-C. Lu, "A CMOS micromachined capacitive tactile sensor with high-frequency output," *J. Microelectromech. Syst.*, vol. 15, no. 6, pp. 1708–1714, Dec. 2006.

[18] J. Wu, G. K. Fedder, and L. R. Carley, "A low-noise low-offset chopper-stabilized capacitive-readout amplifier for CMOS MEMS accelerometers," in *Proc. IEEE ISSCC*, San Francisco, CA, Feb. 2002, pp. 428–478.

[19] C. Wang, M.-H. Tsai, C.-M. Sun, and W. Fang, "A novel CMOS out-of-plane accelerometer with fully differential gap-closing capacitance sensing electrodes," *J. Micromech. Microeng.*, vol. 17, no. 7, pp. 1275–1280, Jul. 2007.

[20] C. Easter and C. B. O'Neal, "Characterization of high-pressure XeF_2 vapor-phase silicon etching for MEMS processing," *J. Microelectromech. Syst.*, vol. 18, no. 5, pp. 1054–1061, Oct. 2009.

[21] G. Zhang, H. Xie, L. E. de Rosset, and G. K. Fedder, "A lateral capacitive CMOS accelerometer with structural curl compensation," in *Proc. IEEE MEMS*, Orlando, CA, Jan. 1999, pp. 606–661.

Ming-Han Tsai was born in Yunlin, Taiwan, in 1982. He received the B.S. and M.S. degrees from the Institute of NanoEngineering and MicroSystems, National Tsing Hua University, Hsinchu, Taiwan, in 2007, where he is currently working toward the Ph.D. degree.

Since 2010, he has been with Pixart Imaging Inc., Hsinchu, as an R&D Engineer for developing CMOS-MEMS physical sensors. His M.S. work used the metal wet-etching approach to implement gap-closing Z-axis CMOS-MEMS accelerometers. His present research interests include CMOS-MEMS inertial sensor design, CMOS multilayer mechanical property extraction, multidomain simulations, post-CMOS fabrication technology, and CMOS-MEMS packaging technology.

Yu-Chia Liu was born in Kaohsiung, Taiwan, in 1985. He received the B.S. degree from the Department of Automatic Control Engineering, Feng Chia University, Taichung, Taiwan, in 2007, and the M.S. degree from the Institute of NanoEngineering and MicroSystems, National Tsing Hua University, Hsinchu, Taiwan, in 2009, where he is currently working toward the Ph.D. degree.

His M.S. work used the polymer fill-in technique to develop a CMOS-based tactile sensor. His present research interests include CMOS-MEMS mechanical sensors and readout circuitry design and post-CMOS fabrication technology.

Weileun Fang (M'06–SM'11) was born in Taipei, Taiwan. He received the Ph.D. degree from Carnegie Mellon University, Pittsburgh, PA, in 1995.

His doctoral research focused on the determination of the mechanical properties of thin films using micromachined structures. In 1995, he was a Postdoctoral Researcher with the National Synchrotron Radiation Research Center, Taiwan. Since 1996, he has been with the Department of Power Mechanical Engineering, National Tsing Hua University, Hsinchu, Taiwan, where he is currently a Professor as well as a Faculty Member of the Institute of NanoEngineering and MicroSystems. In 1999, he was with Prof. Y.-C. Tai at the California Institute of Technology, Pasadena, CA, as a Visiting Associate. His research interests include MEMS with emphasis on microfabrication/packaging technologies, CMOS MEMS, CNT MEMS, microoptical systems, microsensors and actuators, and characterization of thin-film mechanical properties.

Dr. Fang is currently an Editorial Board Member of the *Journal of Micromechanics and Microengineering* and the IEEE TRANSACTIONS ON DEVICE AND MATERIALS RELIABILITY and an Associate Editor of the IEEE SENSORS JOURNAL and *Journal of Micro/Nanolithography, MEMS, and MOEMS*. He has served as the chief delegate of Taiwan to the World Micromachine Summit since 2008 and the General Chair of the World Micromachine Summit 2012. He also served on the Technical Program Committee (TPC) of IEEE MEMS 2004, MEMS 2007, and MEMS 2010, the regional TPC of Transducers 2007, and the Executive Program Committee of Transducers 2009–2013. He has been a member of the International Steering Committee of Transducers since 2009. Moreover, he also serves as a Technical Consultant for many MEMS companies in Taiwan.